Journal of Power Sources 196 (2011) 7117–7125

Contents lists available at ScienceDirect

Journal of Power Sources

journal homepage: www.elsevier.com/locate/jpowsour

Manufacturing and characterization of metal-supported solid oxide fuel cells

Peter Blennow[a,*], Johan Hjelm[a], Trine Klemensø[a], Severine Ramousse[a], Alexander Kromp[b], André Leonide[b], André Weber[b]

[a] Fuel Cells and Solid State Chemistry Division, Risø National Laboratory for Sustainable Energy, Technical University of Denmark, Frederiksborgvej 399, P.O. Box 49, 4000 Roskilde, Denmark

[b] Karlsruher Institut für Technologie (KIT), Institut für Werkstoffe der Elektrotechnik (IWE), Adenauerring 20b, D-76131 Karlsruhe, Germany

ARTICLE INFO

Article history:
Received 28 June 2010
Received in revised form 26 August 2010
Accepted 26 August 2010
Available online 3 September 2010

Keywords:
SOFC
Metal-supported
Redox stability
Electrochemical impedance spectroscopy
Distribution of relaxation times
Complex nonlinear least squares fitting

ABSTRACT

A metal-supported solid oxide fuel cell design offers competitive advantages, for example reduced material costs and improved robustness. This paper reports the performance and stability of a recently developed metal-supported cell design, based on a novel cermet anode, on a 25 cm^2 (1 cm^2/16 cm^2 active area) cell level. An electrochemical performance comparable to state-of-the-art anode-supported cells is demonstrated.

Detailed electrochemical analysis allowed assignment of the overall polarization losses quantitatively to gas diffusion in the metal support, electrooxidation in the anode functional layer, oxygen reduction in the mixed ionic-electronic conducting cathode and an additional polarization process with a rather high relaxation frequency, which may be assigned to an insulating corrosion interlayer.

The durability of the cells was investigated by means of galvanostatic operation for periods of up to 1000 h as well as the dynamic behavior, such as redox-, load- and thermal cycling tests.

The galvanostatic stability tests indicated a fair, but significant degradation rate (~5% decrease in cell voltage/1000 h at 650 °C and 0.25 A cm^{-2}). Furthermore, the metal-supported cells underwent an endurance test of 100 redox cycles at 800 °C without severe degradation nor total failure.

1. Introduction

Solid oxide fuel cells (SOFC) are high-temperature electrochemical devices, which convert the energy of a chemical reaction directly into electrical energy and heat. Due the inherent versatility of the SOFC technology, where high efficiencies can be reached, also for quite small fuel cell units, this technology is attractive for energy conversion systems. Today ceramic anode-supported SOFC cells represent the state of the art with respect to high-temperature fuel cells. Much of the development of SOFC technology has generally been devoted to reduce the thickness of various cell components in order to reduce the operating temperature (below 800 °C), enabling the use of more economical stack and balance-of-plant materials. The various components comprising an SOFC are constantly being refined and improved with the overall aim of achieving higher and more stable electrochemical performance with various fuels, while lowering the cost. Nevertheless, the use of ceramic SOFC cells imposes limits in terms of reliability, cost and ability to handle transients.

Metal-supported SOFC stack technology is believed to offer an alternative to conventional electrode- and electrolyte-supported SOFCs. They have many potential advantages such as good thermal conductivity and ductility of the metallic substrate, which may both improve thermal shock resistance, and lower the internal temperature gradients, allowing quicker start-up [1]. If successful, metal-based SOFC stack technologies have the potential to improve functionality, reliability and reproducibility and reduce the manufacturing cost of SOFC stacks [2], in particular for APU applications which require:

- fast start-up and thermal cycling;
- CO and hydrocarbon rich fuels;
- high current density;
- shock vibration resistance;
- fast transients in electrical loads;
- redox cycling.

Since metal-supported SOFCs have an intrinsically different mechanical behavior, compared to ceramic components, it makes them potential candidates for withstanding the mechanical stresses, e.g. generated by the severe vibrations when a stack is incorporated into systems used for transport applications. Despite these potential advantages, the cell fabrication process has been

* Corresponding author. Tel.: +45 4677 5868; fax: +45 4677 5858.
E-mail address: pebl@risoe.dtu.dk (P. Blennow).

0378-7753/$ – see front matter © 2010 Elsevier B.V. All rights reserved.
doi:10.1016/j.jpowsour.2010.08.088

one of the major challenges holding back the development of metal-supported SOFCs. One of the most important issues is the densification of the electrolyte layer that normally requires high sintering temperatures (normally > 1200 °C for yttria-stabilized zirconia (YSZ)-based electrolytes). These high temperatures tend to lead to serious corrosion of the metallic substrate. To solve the problem, different processing routes to fabricate electrodes and dense electrolytes on metallic supports have been employed, such as atmospheric plasma spray processing (APS) [3,4], vacuum plasma spraying (VPS) [5–8], suspension plasma spraying [9], high-velocity oxy-fuel (HVOF) spraying of liquid suspension feedstock [10,11], pulsed laser deposition (PLD) [12], electrophoretic deposition (EPD) [13], and high-temperature co-sintering in reducing atmosphere [1,14–17].

Most developers of metal-supported SOFCs started out using anodes comprising the conventional cermet of YSZ and nickel, typically used in ceramic anode-supported cells. However, at elevated temperatures in reducing atmospheres, needed for avoiding oxidation of the metal support, nickel exhibit significant coarsening. This leads to loss of triple phase boundaries as well as a decrease in connectivity between Ni-particles, causing a severe degradation of the anode. Furthermore, when Ni-based anodes are used in direct contact with a Fe/Cr-based metal support, the system will suffer from interdiffusion of Ni and Fe/Cr during sintering or during high-temperature operation. Interdiffusion can cause formation of Ni–Cr–Fe alloys or insulating oxides in the anode layer, or result in reduced oxidation resistance and increased coefficient of thermal expansion (CTE) in the support, all which are detrimental to cell performance and stability (see e.g. [2,18] and references therein). Recently, various fabrication techniques and materials have been explored in order to introduce a diffusion barrier layer between a Ni-based anode and the metal support structure, and thereby minimizing the interdiffusion problem [8,17–20].

Based on the abovementioned challenges with interdiffusion in the Ni–Fe–Cr system and Ni coarsening during operation, Risø DTU has developed an unconventional half cell design where these problems can be circumvented by the use of an alternative anode structure [16]. The cell design is based on porous and highly electronically conducting layers into which electrocatalytically active anode materials ($Ce_{0.8}Gd_{0.2}O_{1.9}$, CGO, and minor amounts of Ni) are infiltrated after sintering. This paper presents the performance and stability of the metal-supported cell design developed at Risø DTU on a 25 cm^2 (16 cm^2 active area) cell level, compared with recent results reported on button cells (2 cm × 2 cm, 0.5 cm^2 active area) [16]. The detailed dynamic electrochemical performance of the metal-supported cells has been analyzed in collaboration with Karlsruher Institut für Technologie (KIT/IWE) in Germany.

The approach of using infiltration of various materials for use in metal-supported SOFC electrodes was reported by LBNL [1,15]. Infiltration of Ni and LSM ((La,Sr)MnO_3) into a porous YSZ backbone structure for the use as an anode, and a cathode, respectively, in metal-supported SOFC was successfully demonstrated [1]. They fabricated a five-layer structure consisting of porous metal-support/porous YSZ interlayer/dense YSZ electrolyte film/porous YSZ interlayer/porous metal current collector. The infiltration route avoided undesirable decomposition of LSM, Ni coarsening, and interdiffusion between Ni catalyst and FeCr in the support [1]. However, the power output of a cell with Ni-infiltrated anode degraded rapidly during initial operation. This degradation was attributed primarily to coarsening of the fine infiltrated Ni-particles [15].

The metal-supported cells developed at Risø DTU are intended for operation at lower temperatures in the range 600–750 °C [21]. Furthermore, the cell design is based on a multilayered structure obtainable by conventional low-cost ceramic processing techniques.

2. Experimental

The particle size distribution of the metal powder used in the fabrication of the metal-supported cells was selected to be suitable for tape-casting. The slurries were based on organic solvent and contained, in addition to the Fe–Cr-powder (22% Cr-based stainless steel alloy), binder, plasticizer, and other organic additives necessary for the fabrication process. Some metal-based slurries were also fabricated with 0–50 vol.% Y-doped ZrO_2 (YSZ) with respect to metal powder to, after tape-casting, form a so-called cermet (ceramic + metal) layer. The intention with the layer is to form a backbone structure that can be infiltrated to form the active anode (see below). A similar tape-casting technique was used to fabricate thin electrolyte tapes based on ZrO_2 co-doped with Sc_2O_3 and Y_2O_3 (from here on referred to as ScYSZ). After drying, the tapes were laminated together and cut to desired shape. The final size of the cells is in principle determined by the width of the tape caster (the width of the doctor blade tray) and the sintering shrinkage. The laminated half cells were heat treated in air for debinding followed by co-sintering under proprietary conditions above 1000 °C in reducing atmosphere (H_2/Ar). After co-sintering, the electrocatalytic active phase (to work as fuel electrode) was infiltrated into the porous half cell structure. The infiltration solution comprised precursors for $Ce_{0.8}Gd_{0.2}O_{1.9}$ (CGO20) + 10 wt.% Ni (with respect to CGO20), hereafter referred to as CGO20-Ni. After infiltration, the cells were calcined at 350 °C in air for 2 h. The procedure ensures a uniform coating of nano-sized particles on all the surfaces in the half cell, including the metal support.

As a final step in the fabrication process, the cathode and cathode contact layers were applied by screen printing of $La_{0.58}Sr_{0.4}Co_{0.2}Fe_{0.8}O_{3-\delta}/Ce_{0.9}Gd_{0.1}O_{2-\delta}$ (LSCF/CGO) and $(La_{0.6}Sr_{0.4})_{0.99}CoO_{3-\delta}$ (LSC), respectively, and fired *in situ* during cell testing at the maximum temperature of 800 °C.

A series of cell tests were carried out to measure the performance and durability of the metal-supported cells described above. At Risø DTU, the tested cell had a foot print of 5 cm × 5 cm with an active area of 16 cm^2 (defined by the screen-printed cathode layer). The cell was tested in an alumina housing normally used for conventional anode-supported cells. The test house and positions of voltage probes and current pick-up points have been described elsewhere [22]. The contact components (which also act as gas distribution layers in this set-up) were made from Pt-metal meshes on both the anode and cathode side. The metal meshes form contacts between the cell and the current collector plate that is mounted on the cell test house in contact with the current pick-up and voltage probes. The current pick-up and voltage probes were made from Pt.

Polarization curves were recorded between 650–800 °C with a fuel consisting of hydrogen and 4–20% water on the anode side and air or oxygen (O_2) on the cathode side. Galvanostatic durability testing was carried out in order to assess long-term static stability of the cell. Testing was carried out at low fuel (H_2 + 3% H_2O) and oxygen utilization (<10%), at 650 °C and at a current density of 0.25 A cm^{-2}. The oxidant gas was air. The electrochemical impedance (EIS) measurements were conducted with a Solartron 1260 or a Solartron 1255B frequency response analyzer in the frequency range 0.08 Hz–82.5 kHz (and in some cases in the range 0.17 Hz–383 kHz).

At IWE similar single cells exhibiting an active electrode area of 1 cm^2 (for impedance analysis) and 16 cm^2 (for performance and redox cycling stability tests) were tested in a set-up as described in [23]. The polarization characteristics of the 1 cm^2 cells were investigated at different simulated fuel utilizations (fuel: hydrogen, 5–80% H_2O) and with detailed impedance analysis [24]. Impedance spectra were measured at varying temperatures (500–800 °C), oxidant compositions ($p(O_2)$ = 0.21–2.5 atm) and fuel composition

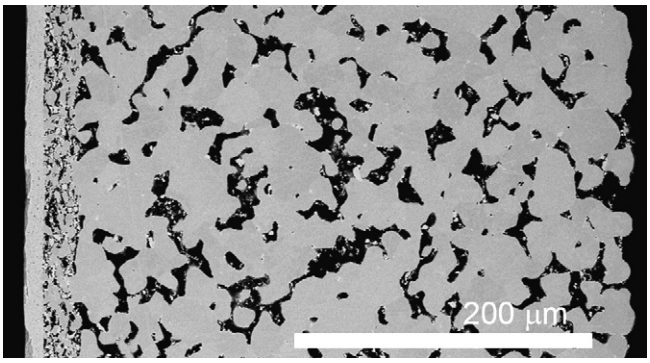

Fig. 1. SEM image showing the polished cross-section of the planar metal-supported half cell before electrocatalyst infiltration and screen printing of cathode. The electrolyte is shown as the dense layer to the left, followed by the cermet layer, and the metal support.

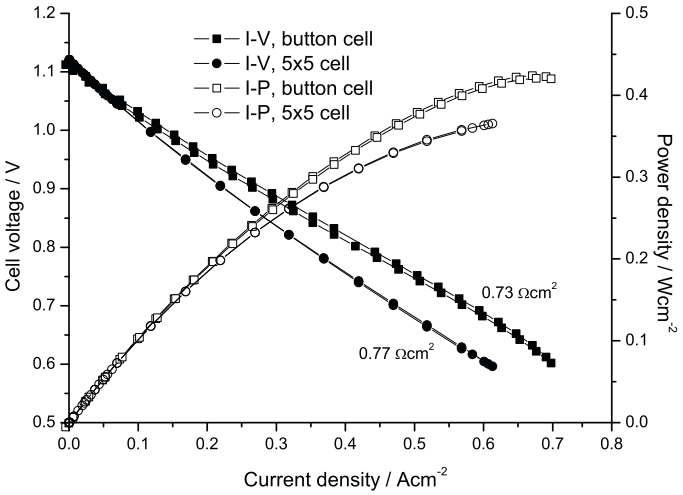

Fig. 2. Electrochemical performance of the metal-supported cells with different foot print sizes (button cell = 4 cm^2 with 0.5 cm^2 active area. 5 × 5 cell = 25 cm^2 with 16 cm^2 active area) at 650 °C (fuel: 96% H_2 with 4% H_2O, oxidant: air). The inserted numbers are the area specific $ASR_{0.6V,secant}$ values calculated for the different cells.

($H_2 + H_2O$, $p(H_2O) = 0.05–0.8$ atm). The spectra were measured under OCV conditions in a frequency range from 100 mHz to 10 MHz. The impedance data analysis was performed by calculating the distribution of relaxation times [25]. For the 16 cm^2 cells the performance was evaluated by means of dc polarization measurements applying the procedures developed within the European projects FCTESTNET and FCTEST^{QA}. The redox stability of the cells was investigated by applying 100 redox cycles with reoxidation times of 1 min (cycle 1–50) and 10 min (cycle 51–100) as described in [26].

The cross-sectional microstructures of the cells were investigated with a Zeiss Supra 25 scanning electron microscope (SEM) equipped with an X-ray energy dispersive spectrometer (XEDS) and with a Hitachi TM1000 tabletop SEM.

3. Results and discussion

A cross-sectional micrograph of a half cell after sintering (before infiltration and testing) is shown in Fig. 1. The micrograph shows that the employed fabrication route gives a metal support layer and a cermet layer that seem sufficiently porous for gas transport. The electrolyte layer in Fig. 1 also seemed to be dense, which was also confirmed during the electrochemical characterization, thereby meeting the requirements of gas tightness.

The amount of infiltrated material in the different samples was calculated by weighing the cells before and after the infiltration step. The total amount of infiltrated material (after calcinations) was measured to be 2.8 ± 0.2 wt.%, corresponding to a Ni content on the anode side of approximately 0.3 wt.%. Since the amount of Ni (NiO) in the infiltrated cells was very small it was difficult to detect any signal with XEDS during the SEM investigation. However, as previous results show [16], there was a dramatic effect on the electrochemical performance with the small additions of Ni to the CGO20 solution. A detailed SEM/TEM analysis is currently in progress and will be reported in a future publication.

3.1. Electrochemical characterization of 16 cm^2 (active area) cells (Risø DTU and IWE)

Fig. 2 shows polarization and power curves recorded at 650 °C, comparing the 5 cm × 5 cm cell with the button cell previously reported [16]. The area specific resistance (ASR) values were calculated as the secant value at 0.6 V and resulted in 0.73 Ω cm^2 and 0.77 Ω cm^2, for the button cell and 5 cm × 5 cm cell, respectively. The polarization curves were conducted at 650 °C with hydrogen (approximately 4% H_2O) as fuel and air as oxidant. Fig. 3 shows the evolution of the cell voltage with time, for the same cells, under a constant current load of 0.25 A cm^{-2} and 650 °C for approximately 1000 h. The degradation rate observed during testing at 0.25 A cm^{-2} was <5%/1000 h, for both cell test protocols, based on the change in cell voltage during the testing period.

The observed performance and the measured degradation rates over 1000 h for the button cell test [16] and the 5 cm × 5 cm test are reasonably close (within 20% of each other) and indicate good correlation between the two different test set-up and contacting protocols. The cell performance results shows generally lower or at least comparable ASR values than that of many other metal-supported SOFCs presented so far in the literature (see e.g. ref. [2] and references therein).

EIS measurements were used to characterize the 5 cm × 5 cm cell at different temperatures (650–750 °C) as well as before and after the galvanostatic durability test at 650 °C. Nyquist and Bode representations of the impedance response in the frequency range 0.08 Hz–82.5 kHz of the cell as a function of temperature are displayed in Fig. 4. A high frequency relaxation process was observed (see Fig. 4) and in the frequency range measured (0.08 Hz–82.5 kHz) no intercept with the real axis can be observed in a complex plane (Nyquist) plot. This makes accurate determination of the serial resistance of the cell difficult. The low frequency end of the impedance spectrum is practically temperature independent, which is consistent with gas concentration related impedances

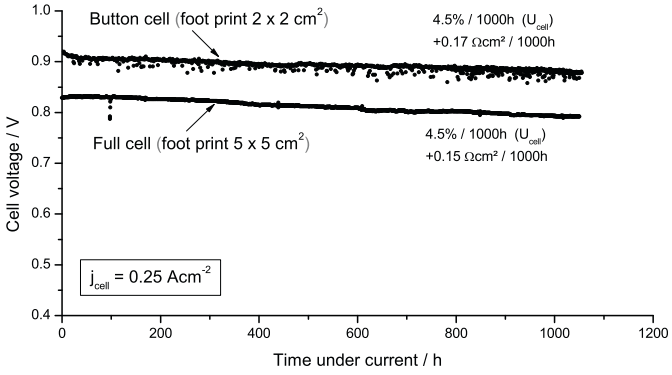

Fig. 3. Galvanostatic durability curves of the metal-supported cells of different foot print sizes tested at 650 °C at a current density of 0.25 A cm^{-2}. Humidified (approximately 4% H_2O) H_2 as fuel and air as oxidant. The button cell results are from ref. [16].

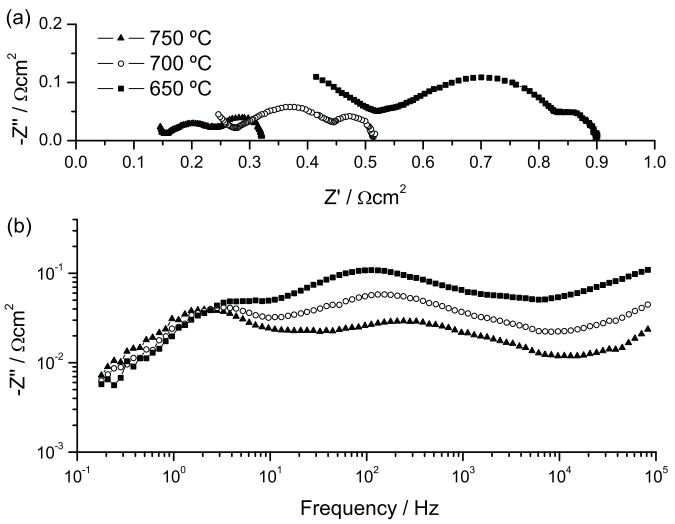

Fig. 4. Nyquist representation (a) and Bode representation of the imaginary part (b) of EIS data recorded at 750, 700, 650 °C with humidified hydrogen as fuel (20% H_2O) and air as the oxidant. The data sets have been corrected for the inductance of the test set-up.

(conversion and diffusion). Similar results were observed when measuring on 1 cm^2 active area cells at IWE (see Section 3.2).

The EIS data recorded before and after the galvanostatic durability testing are displayed in Fig. 5. A wider frequency range during EIS was attempted (0.08 Hz–383 kHz) to try to get an intercept with the real axis. However, as seen in Fig. 5a this was not successful. Higher frequencies are not possible to measure at the current test set-up used at Risø DTU. Therefore, more detailed EIS analysis was conducted in collaboration with IWE, to get a better understanding of this high frequency process (see Section 3.2).

In order to highlight the frequency ranges where the main changes in the impedance spectrum take place as a result of operation under current, a Bode representation of the imaginary part of the complex impedance data is presented in Fig. 5b. Additionally, the calculated ADIS (analysis of differences in impedance spectra [27]) spectrum has been added to the graph.

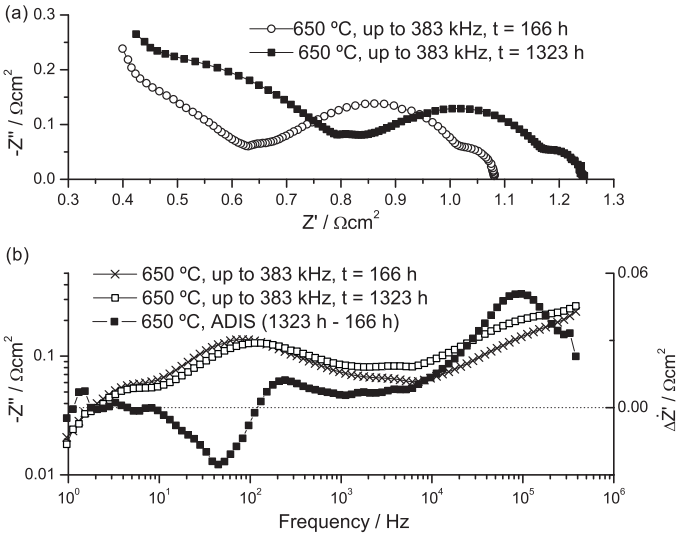

Fig. 5. Nyquist representation (a) and Bode representation of the imaginary part (b) of EIS data recorded before and after galvanostatic durability testing, at a cell temperature of 650 °C and at OCV. The fuel was humidified hydrogen (~20% H_2O) and the oxidant was air. The calculated ADIS difference spectrum (expressed as the quantity $\Delta\dot{Z}'$) is also given in (b) as a function of frequency.

A significant increase in impedance is observed at high frequencies (over 10 kHz), which may be related to changes in the anode functional layer of the cell. A decrease of the impedance in the range 10–100 Hz is observed concurrently, and this may be due to changes to the cathode (which is expected to contribute significantly to the impedance spectrum in this frequency range). The cathode was sintered *in situ*, which might explain the apparent decrease in polarization resistance as the cathode gets a better adhesion to the electrolyte with increased exposure time at 650 °C. The combined results above indicate that the major contributing factor for the degradation during the galvanostatic testing lies in the high frequency region in the EIS. One possible explanation for the increase in ohmic resistance is a formation of a resistive layer, e.g. oxide scale formation on metal particles in the active anode layer, during operation in the fuel atmosphere.

A possible factor causing the degradation/oxidation of the metal particles in the anode layer could be the existence of leaks, either internal or external leaks. Internal leaks are leaks which correspond to permeation of gas from the fuel compartment to the oxidant gas compartment, e.g. by cracks in the electrolyte. External leaks are leaks from a gas compartment to the external atmosphere, e.g. through porosity or holes in the seals.

The quality of the sealing in the 5 cm × 5 cm cell test performed at Risø DTU was assessed by cell voltage measurements at various fuel and oxidant gas flows. Dry hydrogen was used as fuel and air as the oxidant. A so-called equivalent leak current was calculated by calculating how much current is needed to produce the observed cell voltage (lower than the theoretical cell voltage). These leak currents reflect all processes, which consume fuel without generating current, thus taking into account any internal and external leakage, both electronic leakage (short-circuiting) and gas-leakage. More information about similar leak test measurements can be found elsewhere [28]. The leak testing experiments resulted in low leak currents in the range 20–40 mA cm^{-2}. The leak currents were relatively flow independent, indicating that there was no significant pressure driven leaks, such as leaks through large electrolyte cracks or gaps in the sealant material. The leak currents were measured both before and after the galvanostatic durability test, and showed similar results within 20% (the lower values were measured after test), indicating that the degradation in cell performance was not caused by increased leaks in the system.

Fig. 6 displays the performance and OCV degradation of different Ni-YSZ anode-supported cells [26] and a metal-supported cell during 100 Redox cycles. Whereas the anode-supported cells fail

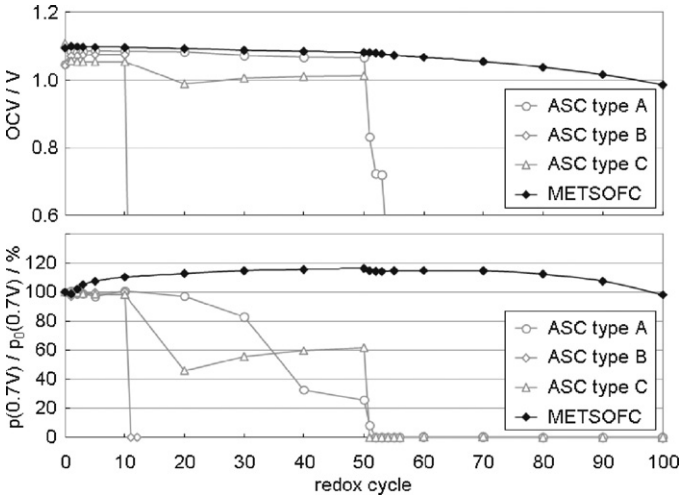

Fig. 6. Redox stability of ASCs (Ni/YSZ anode substrate [26]) and metal-supported SOFCs at 800 °C operating temperature: OCV (top) and relative performance degradation (bottom).

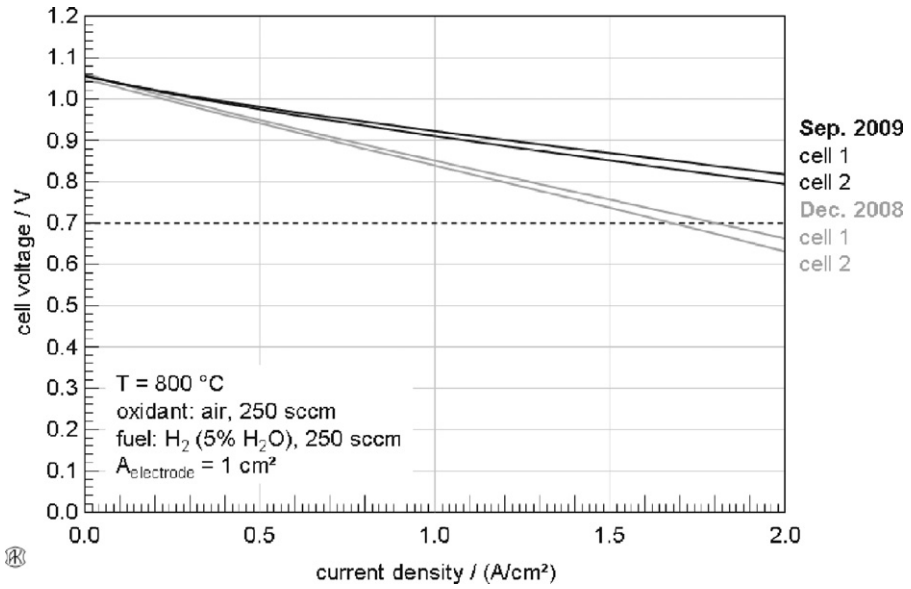

Fig. 7. Polarization characteristics of metal-supported single cells as fabricated in Dec. 2008 and Sep. 2009.

after at least the first 10 min redox cycle (cycle no. 51), the metal-supported cell only shows a slight degradation within cycle 51–100 (10 min redox cycle) and even improves during the first 50 cycles (1 min redox cycle). It is obvious that the metal support is not seriously affected by the reoxidation. The same holds for the CGO20-Ni infiltrated active anode layer (cermet layer). Since the small amount of Ni in the structure only acts as a catalyst and does not form a continuous matrix, the reoxidation neither results in mechanical stress and subsequent cracking of the electrolyte nor in Ni-agglomeration and loss of three phase boundaries.

3.2. Electrochemical characterization of 1 cm² (active area) cells (IWE)

In Fig. 7 polarization characteristics of 2 different generations (generations differ in improved processing understanding of various components of the cell) of metal-supported cells are displayed. It is obvious that a significant performance improvement was achieved during the last year and that the cells of both generations show a performance and reproducibility quite similar to state of the art anode-supported cells tested in the same test bench [29].

In Fig. 8 cell performance is displayed as a function of temperature and H_2O-content (simulated fuel utilization, see [30]) in the fuel. An increase in $p(H_2O)$ from 5% to 80% results in a performance decrease of approximately 50%. The cell performance shows strong temperature dependence, decreasing the operating temperature from 700 to 550 °C results in a decrease in performance of about one order of magnitude.

To investigate the electrochemical processes in the electrodes of the cells, impedance spectra were measured at various operating conditions. The individual loss processes, which are overlapping in the impedance spectra were analyzed by calculating the distribution of relaxation times (DRT) and then quantified with subsequent complex nonlinear least squares (CNLS) fitting [25,31–33]. The importance of electrochemical impedance spectroscopy (EIS) for the ongoing development of SOFCs was recently summarized by Jensen et al. [34]. They presented different methods such as (i) the differential impedance analysis (DIA) [35], (ii) the deconvolution of impedance spectra into DRT first introduced by Schichlein [25] and applied in refs. [31–33,36], and (iii) the analysis of difference in impedance spectra (ADIS) introduced by Jensen et al. [27], Hagen et al. [37], and Barfod et al. [38]. The ADIS method,

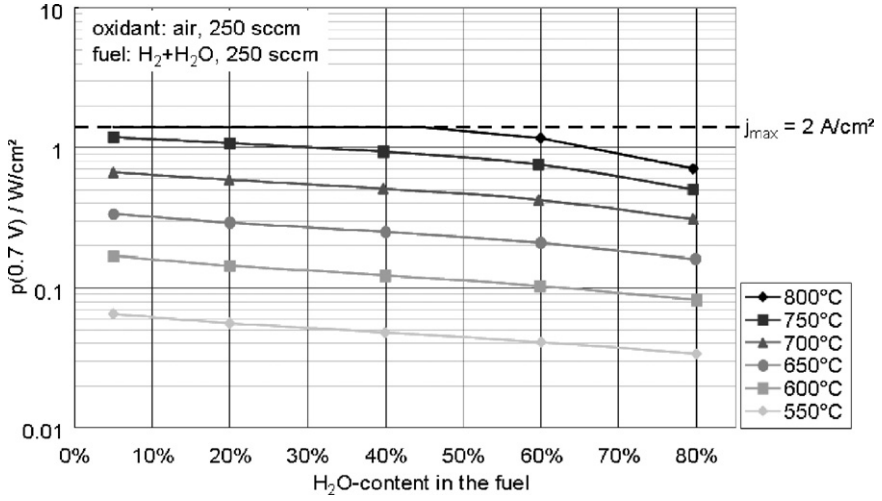

Fig. 8. Power density at 0.7 V cell voltage—impact of temperature and $p(H_2O)$.

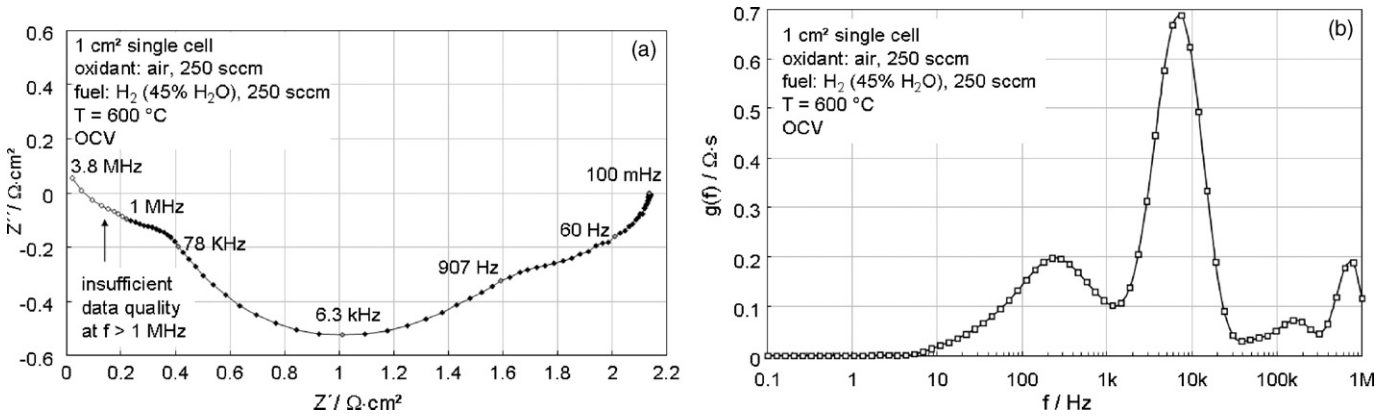

Fig. 9. Impedance spectra (top) and DRT (bottom) of a metal-supported cell.

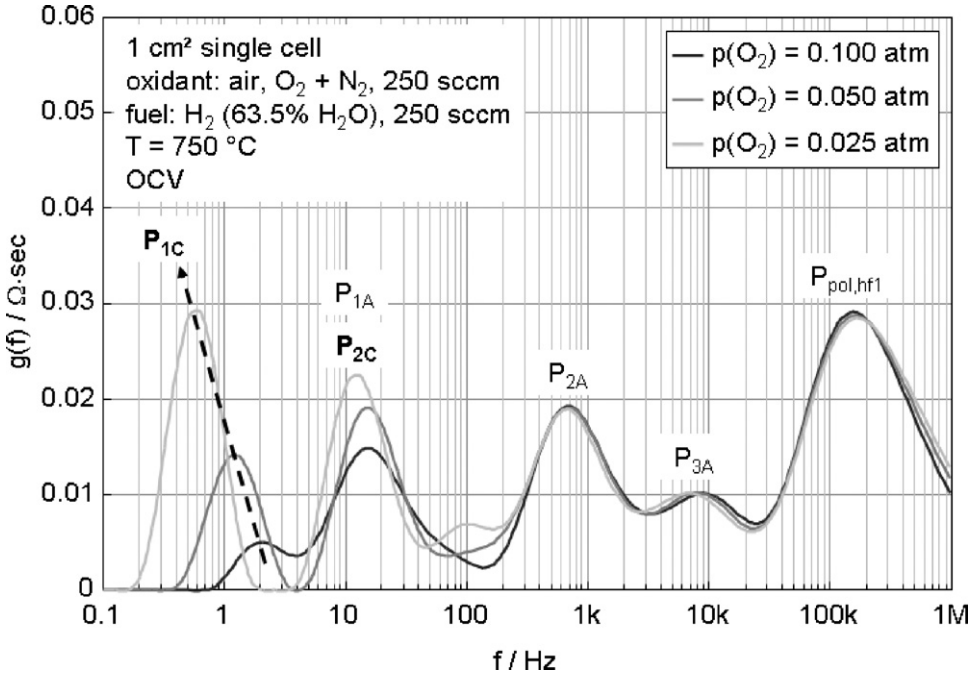

Fig. 10. DRTs of a metal-supported cell at 750 °C—$p(O_2)_{cathode}$ variation.

which has been used to obtain some of the results presented above, analyzes the difference between pairs of impedance spectra measured under different test conditions and distinguishes contributions that completely overlap with other processes. The DIA and DRT methods, instead, are applicable when individual processes show differences in their characteristic DRT. Both methods assist in reducing the number of variables for the CNLS fit. In the following, the DRT method is applied for the pre-identification of the impedance response.

In Fig. 9 an impedance spectra and the related DRT is displayed. Compared to state of the art anode-supported cells, the spectra of the metal-supported cells exhibit additional high frequency processes. Because of the low impedance values, the inductive coupling in the test bench and the limitations of the measuring device (Solartron 1260 A) the impedance values at frequencies above 1 MHz cannot be measured with the required accuracy. Therefore these data points have not been considered in the further impedance data analysis.

In Figs. 10 and 11 the DRTs of a $p(O_2)$ variation at the cathode and a $p(H_2O)$ variation at the anode are displayed for a temperature of 750 °C.

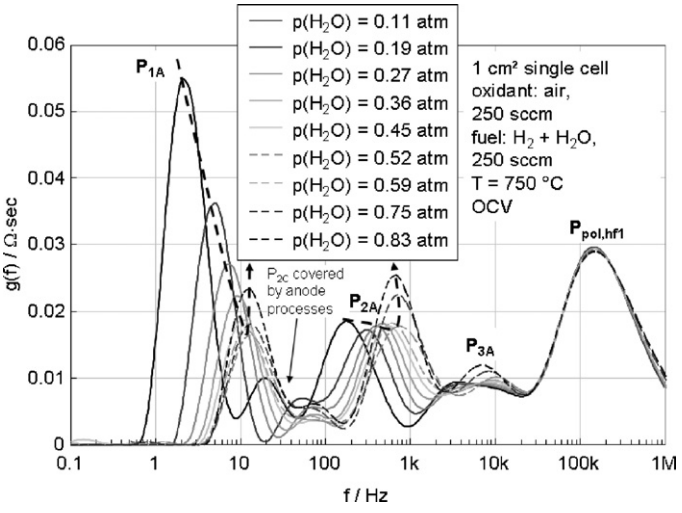

Fig. 11. DRTs of a metal-supported cell at 750 °C—$p(H_2O)_{anode}$ variation.

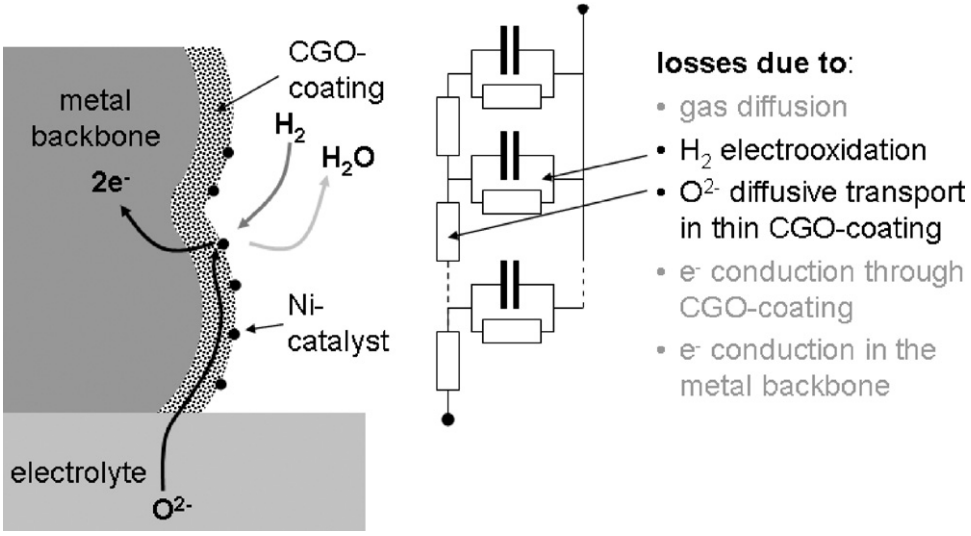

Fig. 12. Sketch of the anode microstructure and corresponding equivalent circuit.

For the cathode a model similar to [39,40] was applied [31]. With decreasing $p(O_2)_{cathode}$, an additional low frequency peak (relaxation frequency 0.8–2 Hz) related to the gas diffusion in the porous cathode layer arises. Using a gold or platinum mesh for current collection and gas distribution (single cell test) and air as the oxidant this process is not observable [41]. Therefore it will not be considered in the further impedance analysis, i.e. the related polarization resistance R_{1C} is estimated to be 0. The main peak for the oxygen reduction reaction in the MIEC-cathode (surface exchange and bulk diffusion described by a Gerischer element [39,40]) exhibits a relaxation frequency of ~10 to 60 Hz, which is consistent with the ADIS results discussed in Section 3.1. However, the rather small impedance of the MIEC-cathode (R_{2C} = 22 mΩ cm^2 at 750 °C in air) is partly overlapped by the processes at the anode.

Similar to state of the art anode-supported cells, at low frequencies a process related to the gas diffusion in the substrate can be described by a generalized finite length Warburg element with the polarization resistance R_{1A} (relaxation frequency of the main peak: 1–20 Hz, Fig. 11) [31]. The processes P_{2A} and P_{3A} related to the H_2 electrooxidation are visible in the frequency range from 100 Hz to 10 kHz.

Taking a look at a schematic of the anode microstructure (Fig. 12), we should take into account that a complex ladder network would be necessary to describe the anode electrochemistry with a physical meaningful model [31,32].

For a quantitative evaluation of the overall polarization resistance of the anode electrochemistry we selected a much simpler approach. H_2 electrooxidation and O^{2-} transport in the CGO-coating was modeled by two processes (P_{2A} and P_{3A}) described by two RQ-elements with the resistance values R_{2A} and R_{3A}. Because there is no physical meaning for R_{2A} and R_{3A}, the polarization resistance of the anode electrochemistry is displayed as the sum of R_{2A} and R_{3A}.

Next to these electrochemical and transport processes, at least one high frequency polarization process has to be considered. This process, further on named $P_{pol,hf1}$ (resistance value $R_{pol,hf1}$), is independent of the fuel and the oxidant gas composition. There are two possible sources of the high frequency contributions, (i) a secondary phase formed in between the LSCF-cathode and the ScYSZ-electrolyte (no ceria interlayer was used) and/or (ii) a corrosion interlayer in between the metal substrate and the infiltrated CGO-interlayer.

A cross-sectional SEM micrograph of the 5 cm × 5 cm cell after test (Figs. 2 and 3) is shown in Fig. 13. The image shows regions where the Fe/Cr particles in the active anode layer (cermet layer—Fig. 1) have experienced some corrosion (formation of Cr-enriched oxides). The image illustrates that the formation of such resistive phases could potentially result in an increase in ohmic resistance after the galvanostatic tests (see Fig. 5) and thereby most likely be related to $P_{pol,hf}$ mentioned above. Further tests are ongoing to understand this phenomenon in more detail.

The CNLS-fit of the impedance data was performed with an equivalent circuit similar to [31] and an additional RQ-element for $R_{pol,hf1}$. The starting values for the fit were estimated from the DRTs. For the fitting of the impedance data series appropriate parameters were kept at a constant value, i.e. in case of the $p(H_2O)$-variations P_{2C} and P_{hf} and in case of the temperature variation the nearly temperature independent gas diffusion polarization in the anode (P_{1A}) was fixed.

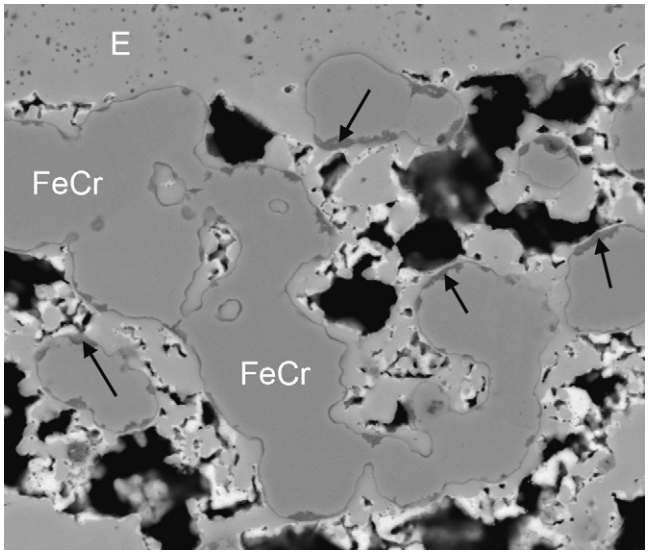

Fig. 13. SEM (back scatter mode) micrograph of the active anode layer after galvanostatic durability test. E denotes part of the electrolyte and FeCr illustrates some of the metal particles in the cermet layer. The dark grey areas (a few pointed out with black arrows) are where the FeCr particles have experienced corrosion during the test. The light grey particles in the cermet layer correspond to the YSZ phase. The infiltrated material (CGO20-Ni) is visible as the bright areas covering all surfaces exposed to the fuel gas in the cermet layer. For more details see ref. [16].

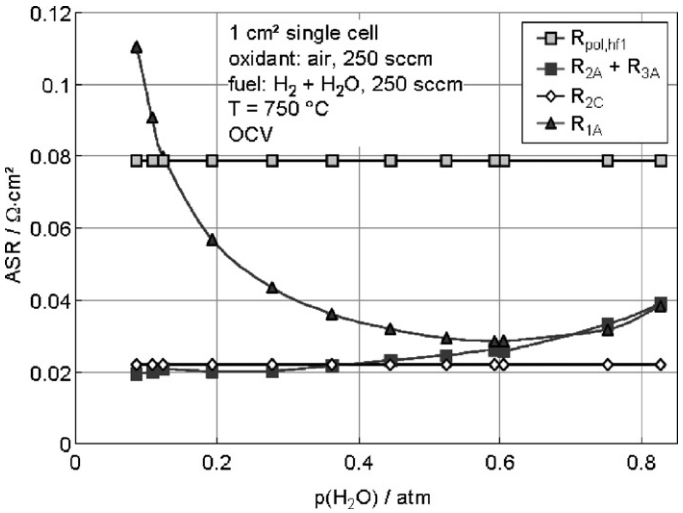

Fig. 14. $p(H_2O)$-dependency of the electrochemical processes at the anode and the cathode at 750 °C.

In Fig. 14 the $p(H_2O)$-dependency of the polarization processes is displayed. Compared to Ni/YSZ cermet anodes [32] the polarization resistance of the infiltrated CGO-anodes given by $R_{2A} + R_{3A}$ is not significantly affected by the $p(H_2O)$. The steep decrease of the polarization resistance with $p(H_2O)$ increasing from ~3% to ~50%, which is well known for Ni/YSZ cermet anodes, was not observed here. The gas diffusion polarization in the metal substrate shows the expected $p(H_2O)$-dependency.

In Fig. 15 the different impedance contributions are displayed vs. the reciprocal temperature. Next to the processes at the cathode, the anode and the high frequency process $P_{pol,hf1}$ an additional high frequency process $P_{pol,hf2}$ is introduced. Due to its high relaxation frequency this process cannot be fitted in the impedance spectra. Therefore $R_{pol,hf2}$ was estimated by subtracting R_{2C}, R_{1A}, R_{2A}, R_{3A}, $R_{pol,hf1}$ and R_{ScYSZ}, the calculated electrolyte resistance of the 12 μm thick ScYSZ electrolyte, from the dc-resistance of the cell. The electrolyte resistance was calculated from 4-point conductivity measurements on sintered pellets of the ScYSZ electrolyte material conducted at Risø DTU. All polarization processes except the gas diffusion in the substrate show an Arrhenius type behavior with apparent activation energies ranging in between 1.13 and 1.34 eV.

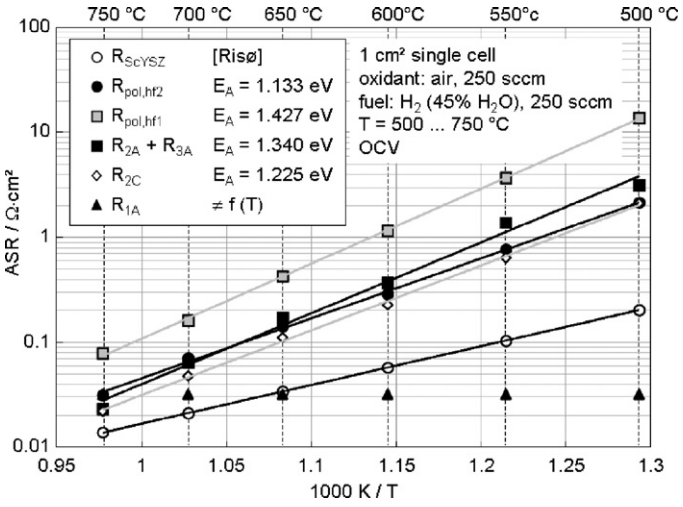

Fig. 15. Temperature dependency of the internal resistance contributions of the metal-supported cell. The resistance contribution from the electrolyte (R_{ScYSZ}) was calculated from 4-point conductivity measurements conducted at Risø DTU on sintered ScYSZ pellets.

Comparing the absolute values and their temperature dependencies with those of a state of the art anode-supported cell [31,42], it becomes obvious that the LSCF-cathode applied in the metal-supported cell exhibits lower polarization resistance values and a lower activation energy. The same holds for the electrooxidation of hydrogen in the infiltrated CGO-anode ($P_{2A} + P_{3A}$). The additional processes with high relaxation frequencies, which neither showed a dependency on the anode nor the cathode gas composition, contribute significantly to the internal resistance of the cell. The performance of the cell is limited by the process $P_{pol,hf1}$, which shows the highest values over the entire temperature range. These resistance contributions can potentially be reduced by adding a ceria interlayer in between LSCF-cathode and ScYSZ electrolyte and by improving the corrosion stability of the stainless steel in the substrate and in the active anode layer.

4. Conclusions

A metal-supported SOFC design has been developed and successfully tested on a 25 cm^2 cell size. The cell design includes an anode structure, in which nano-sized ceria and nickel particles are formed by solution infiltration in the porous microstructure after fabrication of the half cells. The multilayered structure comprising the metal-supported cell was obtained by conventional ceramic processing techniques such as tape-casting, sintering, and screen printing. The cell test results demonstrate fair long-term stability over 1000 h at 650 °C and performance at intermediate temperatures similar or better than conventional Ni-based anode-supported cells. Impedance measurements, DRT-analysis and subsequent CNLS-fitting enabled a separation of the individual polarization mechanisms at the anode and the cathode. Next to the gas diffusion in the metal substrate, the oxygen reduction in the MIEC cathode and the electrooxidation of hydrogen in the anode additional processes, which might be attributed to a secondary phase formed in between the LSCF-cathode and the ScYSZ-electrolyte and/or a corrosion interlayer in between the metal substrate and the infiltrated CGO-interlayer, were observed. These processes have a significant impact on the cell performance.

The developed metal-supported cell design is less sensitive to Ni-agglomeration in the active anode and more robust towards redox cycles. A promising redox tolerance was shown. The metal-supported cells could withstand 100 redox cycles without detrimental degradation. Redox cycling tolerance is important because it allows the cells to e.g. withstand cooling without the need for special protection and interruption in fuel supply. The ability to survive these conditions can reduce balance-of-plant complexity and redundancy. These promising results have justified the first implementation of metal-supported cells (144 cm^2 cell area) into stacks, which will be reported in future publications.

Acknowledgements

Financial support by Topsoe Fuel Cell, the EU project FP7-211940 (METSOFC), and The Danish National Advanced Technology Foundation is gratefully acknowledged. We are thankful to the Fuel Cells and Solid State Chemistry Division at Risø DTU for assistance.

References

[1] M.C. Tucker, G.Y. Lau, C.P. Jacobson, L.C. DeJonghe, S.J. Visco, J. Power Sources 171 (2007) 477–482.
[2] M.C. Tucker, J. Power Sources 195 (2010) 4570–4582.
[3] R. Vassen, D. Hathiramani, J. Mertens, V.A.C. Haanappel, I.C. Vinke, Surf. Coat. Technol. 202 (2007) 499–508.
[4] R. Vassen, H. Kassner, A. Stuke, F. Hauler, D. Hathiramani, D. Stoever, Surf. Coat. Technol. 202 (2008) 4432–4437.
[5] M. Lang, T. Franco, G. Schiller, N. Wagner, J. Appl. Electrochem. 32 (2002) 871–874.

[6] M. Lang, P. Szabo, Z. Ilhan, S. Cinque, T. Franco, G. Schiller, J. Fuel Cell Sci. Technol. 4 (2007) 384–391.
[7] G. Schiller, T. Franco, M. Lang, P. Metzger, A. Stoermer, Meet. Abstr. - Electrochem. Soc. 501 (2006) 1047.
[8] G. Schiller, A. Ansar, M. Lang, O. Patz, J. Appl. Electrochem. 39 (2009) 293–301.
[9] Z. Wang, J.O. Berghaus, S. Yick, C. Deces-Petit, W. Qu, R. Hui, R. Maric, D. Ghosh, J. Power Sources 176 (2008) 90–95.
[10] J. Oberste Berghaus, J.-. Legoux, C. Moreau, R. Hui, C. Deces-Petit, W. Qu, S. Yick, Z. Wang, R. Maric, D. Ghosh, J. Therm. Spray Technol. 17 (2008) 700–707.
[11] R. Hui, J.O. Berghaus, C. Deces-Petit, W. Qu, S. Yick, J. Legoux, C. Moreau, J. Power Sources 191 (2009) 371–376.
[12] R. Hui, D. Yang, Z. Wang, S. Yick, C. Deces-Petit, W. Qu, A. Tuck, R. Maric, D. Ghosh, J. Power Sources 167 (2007) 336–339.
[13] N.P. Brandon, A. Blake, D. Corcoran, D. Cumming, A. Duckett, K. El-Koury, D. Haigh, C. Kidd, R. Leah, G. Lewis, C. Matthews, N. Maynard, N. Oishi, T. McColm, R. Trezona, A. Selcuk, M. Schmidt, L. Verdugo, J. Fuel Cell Sci. Technol. 1 (2004) 61–65.
[14] Y.B. Matus, L.C. De Jonghe, C.P. Jacobson, S.J. Visco, Solid State Ionics 176 (2005) 443–449.
[15] M.C. Tucker, G.Y. Lau, C.P. Jacobson, L.C. DeJonghe, S.J. Visco, J. Power Sources 175 (2008) 447–451.
[16] P. Blennow, J. Hjelm, T. Klemenso, et al., ECS Trans. 25 (2) (2009) 701–710.
[17] T. Franco, M. Brandner, M. Ruttinger, G. Kunschert, A. Venskutonis, L. Sigl, ECS Trans. 25 (2) (2009) 681–688.
[18] M. Brandner, M. Bram, J. Froitzheim, H.P. Buchkremer, D. Stoever, Solid State Ionics 179 (2008) 1501–1504.
[19] P. Szabo, J. Arnold, T. Franco, et al., ECS Trans. 25 (2) (2009) 175–185.
[20] I. Villarreal, M. Rivas, L.M. Rodriguez-Martinez, et al., ECS Trans. 25 (2) (2009) 689–694.
[21] S. Linderoth, J. Electroceram. 22 (2009) 61–66.
[22] S. Singhal, K. Kendall, Chapter 10: Testing of Electrodes, Cells and Short Stacks, High Temperature Solid Oxide Fuel Cells: Fundamentals, Design and Applications, Elsevier Advanced Technology, Oxford, 2003, p. 261.
[23] A. Weber, A. Muller, D. Herbstritt, E. Ivers-Tiffee, Proc. Electrochem. Soc., PV 2001–16 (16) (2001) 952–962.
[24] A. Leonide, V. Sonn, A. Weber, E. Ivers-Tiffee, ECS Trans. 7 (1) (2007) 521–531.
[25] H. Schichlein, A.C. Muller, M. Voigts, A. Krugel, E. Ivers-Tiffee, J. Appl. Electrochem. 32 (2002) 875–882.
[26] A. Weber, in: J. Garche (Ed.), Encyclopedia of Electrochemical Power Sources, Elsevier, Oxford, 2009, pp. 120–134.
[27] S.H. Jensen, A. Hauch, P.V. Hendriksen, M. Mogensen, N. Bonanos, T. Jacobsen, J. Electrochem. Soc. 154 (2007) B1325–B1330.
[28] J.F.B. Rasmussen, P.V. Hendriksen, A. Hagen, Fuel Cells 8 (2008) 385–393.
[29] M. Becker, A. Mai, E. Ivers-Tiffée, F. Tietz, Proc. Electrochem. Soc., PV 2005–07 (2005) 514–523.
[30] A.C. Müller, A. Weber, H.J. Beie, A. Krügel, D. Gerthsen, E. Ivers-Tiffee, Proc. 3rd. Euro. Solid Oxide Fuel Cell Forum, 1998, pp. 353–362.
[31] A. Leonide, V. Sonn, A. Weber, E. Ivers-Tiffee, J. Electrochem. Soc. 155 (2008) B36–B41.
[32] V. Sonn, A. Leonide, E. Ivers-Tiffee, J. Electrochem. Soc. 155 (2008) B675–B679.
[33] C. Endler, A. Leonide, A. Weber, F. Tietz, E. Ivers-Tiffee, J. Electrochem. Soc. 157 (2010) B292–B298.
[34] S.H. Jensen, J. Hjelm, A. Hagen, M. Mogensen, in: W. Vielstich, H.A. Gasteiger, H. Yokokawa (Eds.), Handbook of Fuel Cells: Advances in Electrocatalysis, Materials, Diagnostics and Durability, Volumes 5 & 6, John Wiley & Sons, Chichester, UK, 2009, pp. 792–804.
[35] D. Vladikova, P. Zoltowski, E. Makowska, Z. Stoynov, Electrochim. Acta 47 (2002) 2943–2951.
[36] A.L. Smirnova, K.R. Ellwood, G.M. Crosbie, J. Electrochem. Soc. 148 (2001) A610–A615.
[37] A. Hagen, R. Barfod, P.V. Hendriksen, Y. Liu, S. Ramousse, J. Electrochem. Soc. 153 (2006) A1165–A1171.
[38] R. Barfod, M. Mogensen, T. Klemenso, A. Hagen, Y. Liu, P.V. Hendriksen, J. Electrochem. Soc. 154 (2007) B371–B378.
[39] S.B. Adler, J.A. Lane, B.C.H. Steele, J. Electrochem. Soc. 144 (1997) 1884–1890.
[40] S.B. Adler, J.A. Lane, B.C.H. Steele, J. Electrochem. Soc. 143 (1996) 3554–3564.
[41] M. Kornely, A. Leonide, A. Weber, E. Ivers-Tiffee, ECS Trans. 25 (2) (2009) 815–824.
[42] A. Leonide, Y. Apel, E. Ivers-Tiffee, ECS Trans. 19 (20) (2009) 81–109.